Chapter 1

Introduction

1.1 Introduction

The requirement of miniaturization of electronic components in the semiconductor industry has been the motivation for investigating the properties of thin films based nanoelectronic devices for various electronic, optoelectronic and sensing applications. The thin film technology is a traditional well-established material processing technology commonly used for growing a thin layer of a material ranging from fractions of a nanometer (monolayer) to several micrometers in thickness [Chopra and Kaur (1983), Smith (1994)]. For a thin film (i.e. layer) of a material, the two surfaces of the film are so close to each other that they can have a decisive influence on the internal physical properties and processes of the substance, which in turn, may introduce some new unique properties different from those of its bulk counterpart in the film [Smith (1994)]. As a consequence of the above, the thin film technology is still under development on a daily basis due to its importance in the development of new nanostructure material based nanodevices for various electronic, optoelectronic, gas sensing and bio-sensing applications [Jagadish and Pearton (2006), Wang and Song (2006), Kyoung and Jang (2010), Xu *et al*. (2013)]. The importance of the nanoscale science and technology in the 21st century is clearly evident from the following statement of the US President's advisor for Science and Technology [Moriarty (2001)]:

'*If I were asked for an area of science and engineering that will most likely produce the breakthroughs of tomorrow, I would point to nanoscale science and engineering*'. (*A Lane*, from the introduction to ***National Nanotechnology Initiative: Leading to the Next Industrial Revolution***, US National Science and Technology Council, February 2000).

Now-a-days, thin films and thin film structures in the nanometer range (nanostructures) are objects of large interests for current researchers with their tremendous

applications in the optoelectronic, piezoelectronic and nanoelectronic devices and systems [Wang (2004), Özgür *et al*. (2005), Lu *et al*. (2006), Zhai *et al*. (2009)]. The Greek word "*nano*" means "*dwarf*" [Moriarty (2001), Fang *et al.* (2009)] which translates as "*little man*"; and in metric measurement, 1 nanometer (nm) means 1 billionth (10^{-9}) of any unit. In general, nanostructured materials are defined as the materials whose structural elements—clusters, crystallites or molecules—have dimensions in the 1 to 100 nm range [Moriarty (2001)], which are larger than a molecule but smaller than a microscopic object. The widely accepted definition of the "nanostructure" is a system or object whose at least one dimension is in the order of 100 nm or less [Moriarty (2001), Nalwa (2002)]. In nanostructure thin films, electrons are confined in the nanoscale dimension, but are free to move in other dimensions. Depending on the number of dimensions in the nanoscale range (i.e. 1~100 nm) in which electrons are to move, the nanostructures are classified as follows [Nalwa (2002), Jagadish and Pearton (2006), Tiwari *et al.* (2012)].

- **Zero Dimensional (0D) Nanostructures**: In such nanostructures, all the three dimensions are in the nanoscale range of 1-100 nm. In other words, no dimensions or 0D are larger than 100 nm. The most common example of 0D nanostructures is the arrays of uniformly grown nanoparticles (i.e. quantum dots).

- **One Dimensional (1D) Nanostructures:** If only one out of the three dimensions of a nanostructure larger than 100 nm and other two dimensions are in the nanoscale range of 1-100 nm, the nanostructure is called a one-dimensional (1D) nanostructure. The common examples of 1D nanostructure materials include nanotubes, nanorods, and nanowires. It may be mentioned that 1D nanostructure materials are expected to play important roles in fabricating novel electronic, optoelectronic, and electrochemical energy devices with nanoscale dimensions. The 1D nanostructures are expected to have a tremendous impact in the development of nanoelectronics, nanodevices and systems, nanocomposite materials, alternative energy resources and national security [Tiwari *et al.* (2012)].

- **Two Dimensional (2D) Nanostructures**: In 2D nanostructures, two dimensions are larger than 100 nm and only one dimension is in the nanoscale range of 1-100 nm. The most common examples of the 2D nanostructure are the nanofilms, nanolayers, and nanocoatings. The thin film of any materials grown over large is normally in

the category of 2D nanostructures where two dimensions other than the film thickness are larger than 100 nm.

- **Three Dimensional (3D) Nanostructures:** In 3D nanostructures, none of dimensions are in the nanoscale range and hence electrons are not confined in none of the directions. Dispersions of nanoparticles, bundles of nanowires, and nanotubes as well as multi nanolayers can be considered as the example of 3D nanoparticles.

Among various semiconducting materials, nanostructures of zinc oxide (ZnO) can be special interests to many due to its many important properties for transport electronics [Klingshirn (2007)], blue/Ultraviolet (UV) optoelectronics [Jagadish and Pearton (2006)], spintronics [Pearton *et al*. (2006)], gas sensing [Sadek *et al*. (2007)], piezoelectronic [Wang and Song (2006), Wang (2012)], biomedical [Zhang *et al.* (2013)] and bio-sensing [Xu *et al*. (2013)] applications. Despite the similar electronic properties with a direct energy bandgap of 3.37 eV of ZnO and GaN, the ZnO is normally preferred over the most commonly used GaN for UV detection applications because of its lower cost, varieties synthesis techniques including the low-cost thermal evaporation and sol-gel methods for growing various ZnO nanostructures on a large number of substrates including plastics, glass, Si, sapphire (Al_2O_3), diamond etc., completely environment-friendly nature, and larger excitonic binding energy of ~60 meV of ZnO as compared to the ~25 meV excitonic energy of GaN material. Due to the large direct bandgap (~3.37eV) and high exciton binding energy (~ 60 meV) [Jagadish and Pearton (2006), Janotti and Walle (2009)], ZnO can easily be used for the source and detector applications for operations in the UV region. ZnO can be made to possess a number of intrinsic and extrinsic radiative defect levels which can enable it to emit light in a wide range even within the visible region [Van de Walle (2001), Djurišić *et al*. (2007)]. The structural, electronic, magnetic and optical properties of ZnO are reported to be easily tailored through doping, alloying and nano engineering [Jagadish and Pearton (2006)]. The ZnO material can also exhibit ferromagnetism property when it is doped with transition metal such as Mn at the practical curie temperatures [Jagadish and Pearton (2006)]. Most importantly, the ZnO material has a natural tendency for self-organized growth which can be explored for growing various ZnO nanostructures such as nanowires, nanotubes, nanorods, nanobelts, nanofilms, nanoparticles etc. [Wang (2004)]. One of the major focuses in the current nanoscience and technology research is to explore the shape and size of various ZnO nanostructures in

optimizing the performance of the ZnO nanostructure based electronic and optoelectronic devices [Solomon (2000), Özgür *et al*. (2005), Zhai *et al*. (2009)] As a consequence, the ZnO nanostructures based electronic devices have an innovatory impact on the current semiconductor industry. The ZnO nanostructures based devices grown on the Si substrates may provide addition boost in the development of future generation smart ZnO based nanoscaled electronic devices because of their inherent flexibility of possible integration with the well-matured CMOS technology.

A number of ZnO nanostructure based devices such as the large area Schottky diodes [Kim *et al*. (2008), Singh *et al.* (2011)], nano-contact Schottky diodes [Das *et al.* (2010a), Periasamy and Chakrabarti (2011)], heterojunction diodes [Ajimsha (2008), Shao *et al*. (2012)], homojunction diodes [Özgür *et al*. (2005)], thin film transistors [Park *et al.* (2004), Fortunato *et al*. (2005)] nanogenerators [Wang and Song (2006)] etc. have already been reported. In view of the enormous importance of the ZnO nanostructure based electronic and optoelectronic devices, the present thesis has been developed to mainly focus on the fabrication and characterization of some ZnO nanostructure based devices grown on Si substrates by the simple and low-cost thermal evaporation method. The following sections have been designed to provide the basic information related to the electronic, structural and optoelectronic properties of ZnO, various ZnO nanostructures, and the potential applications of ZnO nanostructures. The basics of ohmic and Schottky contacts grown on ZnO material for various device fabrication are also discussed. Finally, the scopes of the present thesis have been outlined at the end of this chapter.

1.2 General Properties of ZnO Material

The ZnO, also known as *pompholyx* and *lana philosophica* (philosopher's wool) is a II-VI semiconductor material, is regarded as one of the best suitable candidates for short wavelength optoelectronic applications [Klingshirn (2007), Lee (2008), Biswas (2010)]. However, ZnO is not a new material derived from complex material engineering; instead it has been a material well-known for centuries [Dioscorides (1st Century), Brown (1976), Lee (2008)]. Even students studying basic chemistry are also familiar with the common textbook reaction as an example of a combustion reaction [Lee (2008)]:

$$2Zn(s) + O_2(g) \rightarrow 2ZnO(s) \quad (1.1)$$

Since the present thesis deals with the nanoscaled devices of ZnO nanostructures, we have presented some basic properties ZnO in this section as follows.

1.2.1 Structural Properties

ZnO is an II-VI compound semiconductor whose ionicity resides at the borderline between covalent and ionic semiconductor [Jagadish and Pearton (2006)]. The crystal structures shared by ZnO are wurtzite, zinc blende, and rock salt. At ambient conditions, the thermodynamically stable phase is wurtzite [Bunn (1935)]. The stable zinc-blende structure can only be achieved by growing ZnO on cubic substrates. The rocksalt NaCl structure may be obtained at relatively high pressures [Jagadish and Pearton (2006)]. The wurtzite structure has a hexagonal unit cell with two lattice parameters a_0 and c_0 in the ratio of $c_0 / a_0 = 8/3 = 1.633$ and belongs to the space group of C_{6V}^4 or $P6_3mc$. A schematic representation of the wurtzite ZnO structure is shown in Fig. 1.1.

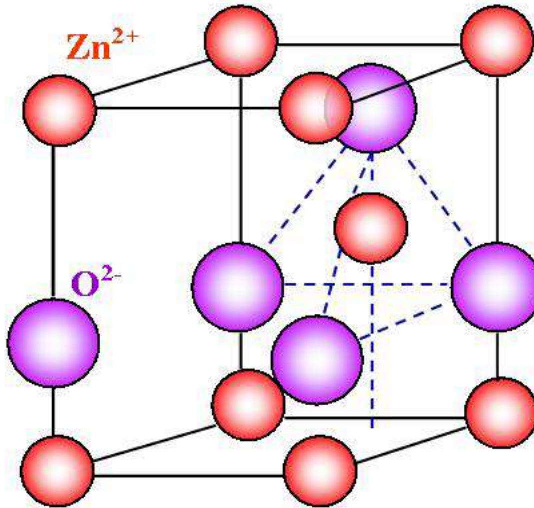

Figure 1.1: Wurtzite hexagonal crystal structure of ZnO [www.nanoscience.gatech.edu]

The wurtzite crystal structure of ZnO is composed of two interpenetrating hexagonal-close-packed (hcp) sublattices, each of which consists of one type of atom displaced with respect to each other along the threefold c_0-axis by the amount of $u = 3/8 = 0.375$ (in an ideal wurtzite structure) in fractional coordinates where the u parameter is defined as the length of the bond parallel to the c_0 axis expressed in the

units of c_0 [Jagadish and Pearton (2006)]. Each sublattice includes four atoms per unit cell and every atom of one kind (group-II atom) is surrounded by four atoms of the other kind (group VI) or vice versa, which are coordinated at the edges of a tetrahedron [Jagadish and Pearton (2006)]. The large electro-negativity difference between the zinc and oxygen atoms makes the Zn-O bond strongly polarized and that strong bond polarity places ZnO in the middle between pure covalent and pure ionic crystals [Özgür *et al*. (2005), Lee (2008)]. Thus, ZnO inherits many advantageous properties of being an ionic crystal. As an example, the near ionic character of ZnO implies that human body can absorb ZnO as Zn and O ions [Lee (2008)]. Since both the Zn and O ions are non-toxic, the material could be very useful for consumer areas, especially in the biotechnology applications [Lee (2008)].

1.2.2 Electronic Band Structure of ZnO

The electronic band structure of a semiconductor provides the basic electronic properties based on which the potential utility of the material is determined. The band structure gives the electronic one-particle (i.e. electron or hole) states [Janotti and Walle (2009), Schifano (2009)] of the material. For any semiconductor, this structure is such that the filled valence band is separated from an empty conduction band by a band gap containing no allowed states at 0 ºK [Zwicker and Jacobi (1985)]. The band structure of ZnO is shown in Fig.1.2 along high symmetry lines in the hexagonal Brillouin Zone [Jagadish and Pearton (2006)].

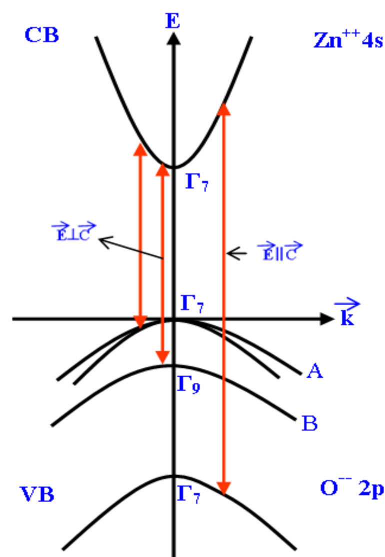

Figure 1.2: The valence band and conduction band of ZnO separated by fundamental band gap

Both the valence band maxima and the lowest conduction band minima occur at the Γ point at k = 0 indicating that ZnO is a direct band gap semiconductor [Zwicker and Jacobi (1985)]. The band gap of ZnO is 3.44 eV at low temperatures and 3.37 eV at room temperature [Jagadish and Pearton (2006), Janotti and Walle (2009)]. The experimental techniques which can be used to determine band structure of ZnO is UV induced photoemission spectroscopy, X-ray induced photoemission spectroscopy and angular photoelectron spectroscopy.

1.2.3 Optical Properties of ZnO

As mentioned earlier that ZnO is a wide band gap (~3.37 eV), II-VI compound semiconductor suitable for photonic applications in the UV or blue spectral range [Djuriˇsi'c´ and Leung (2006), Zhai *et al*. (2009)]. The high exciton binding energy of ~60 meV of ZnO material [i.e. 2.4 times larger than that of the GaN (~25meV)] can ensure the efficient excitonic emission at room temperatures. The wide band gap of ~3.37 eV allows more than 80% transmission in the visible and near infrared wavelength range. This property of ZnO has made it an important material for the visible blind UV detector and transparent conductive contacts in solar cell applications [Chopra *et al*. (2004), Xu and Sun (2011), Xu *et al*. (2014)]. A number of experimental techniques are available for studying the optical transition properties such as reflection, photo-reflection, transmission, UV-Visible optical absorption, photoluminescence (PL), cathodoluminescence (CL), spectroscopic ellipsometry and calorimetric spectroscopy of the ZnO material.

It may be mentioned that GaN (with bandgap of ~3.4 eV and exciton binding energy of ~25 meV) is the most commonly used material in the lighting industry for the production of blue, UV and white light emitting devices [Allen (2008), Zhai *et al*. (2009)]. However, ZnO has been a good contender to GaN for optoelectronic applications in the blue/UV/visible range because of its 2.4 times larger exciton binding energy than that of the GaN which may lead to brighter light emission and exciton-recombination UV lasing at room temperature [Allen (2008)].

Further, the low-cost growth of the single crystal ZnO, its environment-friendly, bio-compatible nature, and the availability of wet etching technique for ZnO can also make the ZnO a better material than the GaN for low-cost electronic and optoelectronic applications as discussed earlier.

1.2.4 Native Point Defects and Doping in ZnO

The understanding of nature of native point defects such as vacancies, interstitials, and antisites etc. in ZnO material is of vital importance as it determines its use in practical applications [Janotti and Walle (2006), Sokol *et al*. (2007)]. These native point defects are responsible for self-diffusion and also assist impurity diffusion, therefore playing a major role in growth, processing, and device degradation [Janotti and Walle (2006), Selim *et al*. (2007)]. As-grown ZnO is always n-type and this unintentional n-type conductivity has often been attributed to the presence of different native defects such as Zn interstitials (Zn_i), oxygen vacancies (O_i) etc. in the band gap of ZnO material [Janotti and Walle (2006), Sokol *et al*. (2007)].

Typically, the photoluminescence spectrum of ZnO exhibits a near-band-edge UV emission due to the recombination of free excitons and a broad defect related visible emission [Reynolds *et al*. (1996), Djurišić and Leung (2006), Gong *et al.* (2007)]. These defect-related broad visible emissions commonly belong to the green luminescence [Gong *et al.* (2007)]. Although other emissions such as yellow or blue have also been observed, however, the origin of defect emissions is not yet fully clear in ZnO material [Van de Walle (2001), Gong *et al.* (2007), Djurišić *et al*. (2007)]. For device applications, such as high efficiency UV light emitting devices and photodetectors, it is significantly important to suppress the emission in the visible range. Thus, it is utmost important requirement of current researchers to develop novel methods for suppressing deep level defect emissions in the ZnO materials for optoelectronic applications in the UV range.

The typical defects occurring in ZnO are listed in Fig.1.3 where the Zn_i and O_i are self-interstitials resulted from the same type of atoms acting as the host, and Q_i is used to denote the interstitials involving an impurity level as the host [Schifano (2009)]. For example, if an impurity, say Q_i occupies a sub-situational lattice site in ZnO and replace a Zn or an O atom, then it forms the Q_{Zn} or Q_O respectively. The Zn and O lattice sites can also be vacant and form a vacancy named V_{Zn} and V_O respectively. Finally, the above mentioned defects can combine together to form higher order complexes [Selim *et al*. (2007), Schifano (2009)]. However, among all the defects, the defects favored by Zn-rich conditions (V_O and Zn_i) may behave as donors. It may be noted here that the oxygen vacancies have the lowest formation energy and hence they are frequently invoked as the

source of n-type conductivity in ZnO [Van de Walle (2001), Djuriˇsi´c *et al*. (2007), Schifano (2009)].

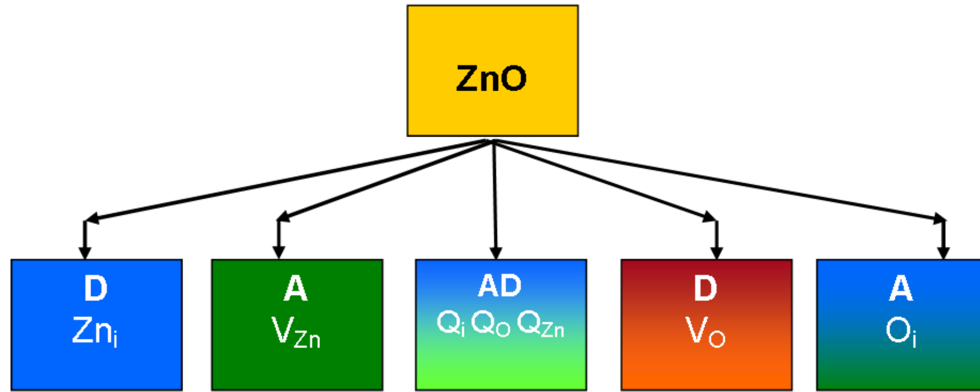

Figure 1.3: Summary of the point defects that may occur in ZnO, where A and D stand for acceptor and donor respectively

It is important to mention here that the properties of the defects and impurities in ZnO are still not clearly understood and hence their proper characterizations are still not possible with certainty [Zhang *et al*. (2001), Bayan and Mohanta (2011)]. This imposes a major restriction in achieving stable metal/ZnO Schottky diodes used for studying the deep level defects in semiconductors by junction spectroscopy techniques like admittance spectroscopy (AS) and deep level transient spectroscopy (DLTS) [Brillson *et al*. (2007), Djurišić *et al*. (2007)].

In ZnO, group III elements like Al, Ga and In on Zn site may form Al_{Zn}, Ga_{Zn} and In_{Zn} defects acting as donors in ZnO which can lead to the intrinsically high n-type conductivity of ZnO and its transparency to light in the visible wavelength range [Schmidt-Mende and MacManus-Driscoll (2007), Schifano (2009)]. Hydrogen is another well known impurity which can also yield *n*-type conductivity in ZnO with a donor level ~50 meV below the conduction band-edge (E_C) [Schifano (2009)]. The known extrinsic acceptors in ZnO include group I elements on Zn site, such as the Li_{Zn}, Na_{Zn} and K_{Zn} and group V elements on O site like N_O, P_O, As_O and Sb_O [Look and Claflin (2004), Look (2006), Schifano (2009)]. However, the development of reliable p-type doping for ZnO material is still a challenge to the researchers because of the self-compensation from native donor defects and/or hydrogen incorporation [Look and Claflin (2004), Look (2006)]. As a

consequence, the synthesis of stable p-type ZnO has been still a challenge despite some progresses already reported in the literature [Schifano (2009), Zhang *et al*. (2001)].

Table.1.1: Physical properties of Zinc Oxide

Property	Value
Molecular Formula	ZnO
Apperance	Amorphous white or yellowish white powder
Stable phase at 300 K	Wurtzite
Melting point	1975 °C
Boiling point	2360 °C
Solubility in water	0.16 mg/100mL
Lattice parameters at 300 K	a_0 = 0.32495 nm, c_0 =0.52069 nm
a_0 / c_0 (*)	1.602 (ideal hexagonal structure shows ~1.633)
u	0.345
Density	5.606 g cm^{-3}
Refreactive index	2.008, 2.029
Static dielectric constant	8.656
Thermal conductivity	0.6,1-1.2
Linear expansion coefficient	a_0 : 6.5×10^{-6} , c_0 : 3.0×10^{-6}
Intrisic carrier concentration (per cm^3)	10^{16} to 10^{20}
Energy bandgap	3.37 eV Direct
Typical defects	Zinc interstitials, Oxygen vacancies, zinc vacancies
Exciton binding energy	60 meV
Electron effectve mass	0.24 m_0
Electron Hall mobility at 300K	200 cm^2 V^{-1} s^{-1}
Hole effective mass	0.59 m_0
Hole Hall mobility at 300K	5-50 cm^2 V^{-1} s^{-1}
Typical impurities	H, Al, In, Ga.

1.3 Nanostructures of ZnO

The ZnO material has diverse nanostructures whose configurations are much richer than any known nanomaterials including carbon nanotubes [Wang (2004), Jagadish and Pearton (2006)]. Fig.1.4 shows the field emission scanning electron microscopy (FESEM) images of different ZnO nanostructures such as nanowires [Ngo-Duc *et al*. (2012)], nanorods [Chae *et al.* (2010)], nanotubes [Tang *et al*. (2007)], nanoparticles [Singh and Nakate (2013)], nanohelixes [Wang (2004)], nanorings [Wang (2004)], nanocombs [www.phy.mtu.edu], nanobelts [Xu *et al*. (2008)], nanotetrapods [Jin *et al*. (2013)], and

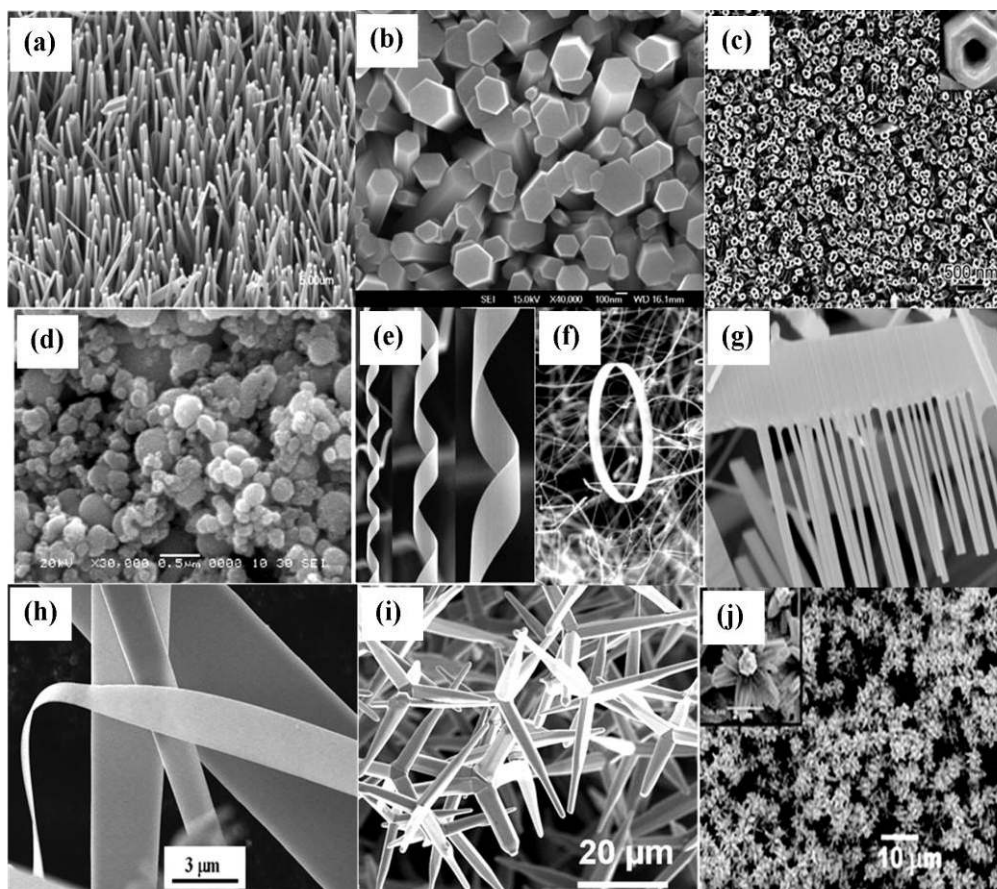

Figure 1.4: FESEM images of different ZnO nanostructures reproduced from the published literature including **(a)** ZnO nanowires [Ngo-Duc *et al*. (2012)] **(b)** ZnO nanorods [Chae *et al.* (2010)] **(c)** ZnO nanotubes [Tang *et al*. (2007)] **(d)** ZnO nanoparticles [Singh and Nakate (2013)] **(e)** ZnO nanohelixes [Wang (2004)] **(f)** ZnO nanorings [Wang (2004)] **(g)** ZnO nanocombs [www.phy.mtu.edu] **(h)** ZnO nanobelts [Xu *et al*. (2008)] **(i)** ZnO nanotetrapods [Jin *et al*. (2013)] **(j)** ZnO nanoflowers [Xu and Sun (2011)] etc.

nanoflowers [Xu and Sun (2011)] synthesized under various specific growth conditions reported in the literature. In general, the ZnO nanostructures have larger surface area to volume ratio than their bulk counterparts, which can be explored for UV detection and gas sensing applications [Huang and Choi (2007), Zhai *et al*. (2009)].

1.4 Synthesis of ZnO Nanostructures

It is discussed earlier that the low-dimensional ZnO nanostructures are of great interests for fundamental research of nanoelectronic devices for future generation detection and sensing applications due to their unique structural, chemical and physical properties entirely different from their bulk counterparts [Nalwa (2002), Fan *et al*. (2006), Guozhong and Ying (2011)]. As a consequence, the synthesis of ZnO nanostructures in an effective and controllable manner has become the most challenging issue for the researchers working with the ZnO nanostructures.

A large variety of ZnO deposition techniques have been reported for the synthesis of ZnO nanostructures [Lu *et al*. (2006), Jagadish and Pearton (2006)]. The most notable methods are chemical vapor deposition (CVD), vapor phase transport (VPT), molecular beam epitaxy (MBE), pulse laser deposition (PLD), Radio frequency (RF) sputtering, sol-gel and thermal evaporation (TE) methods [Smith (1994), Wang (2004), Özgür *et al*. (2006), Lu *et al*. (2006), Li *et al*. (2008), Biswas (2010)] on varieties of substrates including Si [Wang *et al*. (2007), Hwang *et al*. (2012)], sapphire [Kim *et al.* (1997)], GaN [Wei *et al*. (2013)], GaAs [Ma *et al*. (2005)], Indium Tin Oxide (ITO) coated glass [Lee *et al.* (2011)], and polymers [Yao *et al.* (2012)] materials. However, the thermal evaporation is perhaps the most cost-effective and user friendly physical vapor deposition (PVD) technique suitable for the fabrication of large varieties of ZnO nanostructures (in the form of high-quality ZnO thin films with thicknesses in the order of nanometers) on various substrates including glass, plastic, films, metals, and almost any other kind of materials by just changing the growth conditions and operating parameters of the deposition unit [Yao *et al*. (2002), Jagadish and Pearton (2006)].

For the reliable applications of ZnO nanostructure based devices, it is very important that the growth of the ZnO nanostructures is repeatable and cost effective [Lu *et al*. (2006), Wang *et al*. (2008)]. Further, the epitaxial orientation relationship between the ZnO and the substrate material (on which ZnO film is to be deposited) must be such that

the well-aligned ZnO nanostructure can grow perpendicular to the surface of the substrate [Logeeswaran *et al*. (2011)]. In general, suitable self-assembly techniques are opted for the growth of ZnO nanostructures on any substrate as a better choice over the conventional processing techniques such as spray, roll, and spin coating method [Özgür *et al*. (2006), Lu *et al*. (2006), Jagadish and Pearton (2006)]. Further, the self-assembly technique can also be combined with the area-selective growth of the ZnO film on metal catalysts or other seed/buffer layers to achieve a degree of positional control in addition to alignment of the nanostructures [Jagadish and Pearton (2006), Sun *et al.* (2008), Logeeswaran *et al*. (2011)]. However, the major difficulty in large scale integration of ZnO thin film based electronics and optoelectronics devices is the identification of a unitary substrate material due to the poor compatibility of ZnO with the most commonly used Si substrate in modern day's semiconductor technology [Logeeswaran *et al*. (2011)]. Although, an intense debate is always there whether to integrate the high-performance optoelectronics on Si, Indium Phosphide (InP), or GaAs, but that contest can't not weaken the domination of Si as substrate material in the integrated circuits (ICs) technology [Logeeswaran *et al*. (2011)]. In fact, the domination of Si in modern CMOS technology has motivated the researchers [Logeeswaran *et al*. (2011)] for developing the ZnO nanostructure based devices on the Si substrates for achieving future generation smart devices and systems for optoelectronic and gas sensing applications.

In general, sapphire is the preferred substrate [Sun and Kwok (1999), Zhang *et al*. (2004), El-Shaer *et al*. (2005)] for the growth of ZnO nanostructures due its electrically insulating nature. However, difficulty in cleaving causes the complexity of subsequent device integration [Wang *et al*. (2007)]. On the other hand, large-area high-quality single crystal Si wafer is easily available as a low-cost substrate material with well-matured processing technology. Thus, synthesis of ZnO nanostructures on Si substrates is no doubt an interesting area of research. However, the easy oxidation of silicon surface, the formation of silicides even at room temperature, and the large lattice mismatching between ZnO and Si can affect severely the quality of ZnO films grown on Si substrates [Fu *et al*. (1998), Shen *et al*. (2006), Wang *et al*. (2007)]. To overcome these issues, researchers normally use a seed layer of different material on the Si substrate prior to the growth of the ZnO film on it [Shen *et al*. (2006), Wang *et al*. (2007), Zhao and Hu (2009)]. Seed layer or buffer layer is term typically refers to a layer sandwiched between two single-crystal materials to accommodate the difference in their crystallographic structures (lattice

constants) [Guozhong, and Ying (2011)]. A number of researchers have reported the seed layers of different materials such as Zn [Fu *et al*. (1998)], MgO [Wang *et al*. (2007)], ZnO [Song and Lim (2007), Hwang and Chen (2012)], Al_2O_3 [Shen *et al*. (2006)], Al doped ZnO (AZO) [Lee *et al*. (2011)] etc.

1.5 ZnO Thin Film Characterization Techniques

Thin films material characterization is an integral part of the nanoelectronic devices. In this section we will briefly discuss the working principles of some important material and thin film characterization techniques used for investigating the structural, optical and electrical characteristics of ZnO thin films and their devices considered in this present thesis.

1.5.1 Field Emission Scanning Electron Microscopy (FESEM)

The electron microscope is a type of microscope used to magnify objects on a very fine scale. It uses a particle beam of high energy electrons to illuminate a specimen, and create a highly-magnified image. The scanning electron microscope (SEM) is a type of electron microscope that builds up the images of the sample's surface point by point in a time sequence by scanning it with a high-energy beam of electrons in a raster scan pattern.

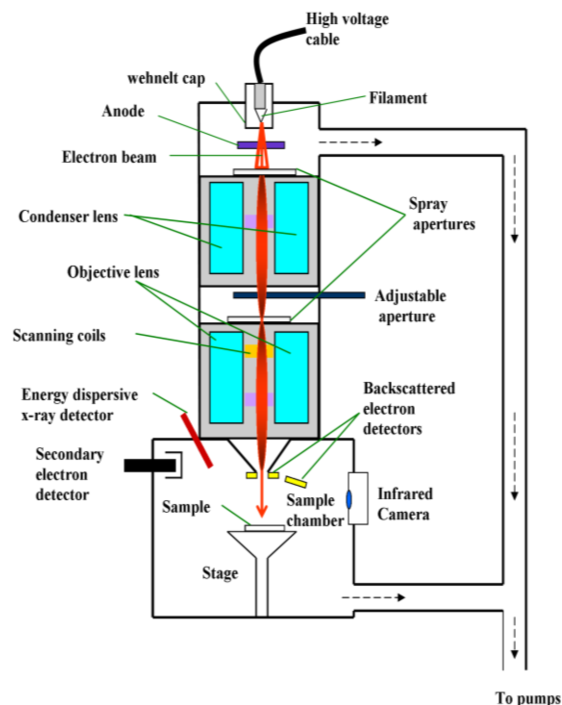

Figure 1.5: Schematic diagram of Scanning Electron Microscopy

Fig.1.5 shows the schematic diagram of SEM unit. The electrons interact with the atoms that make up the sample and produce signals containing the information about the sample's surface topography, composition and other properties such as the electrical conductivity. A field emission SEM (FESEM) is a type of SEM where a field-emission cathode in the electron gun of a SEM provides narrower probing beams at low currents as well as high electron energy, resulting in both improved spatial resolution and minimized sample charging, and damage. It is used for applications which demand the highest magnification possible. Both FESEM and ordinary SEM with a thermionic gun source have been used for investigating the surface morphology of the ZnO thin films considered in the present thesis.

1.5.2 Energy Dispersive X-ray Spectroscopy (EDS)

Energy dispersive X-ray (EDX) or (EDS) is an analytical technique used to extract the information about a specimen composition from its X-ray emission. For this purpose, an EDX detector is installed as an integrated part of SEM. Thus employing the scanning ability of the SEM, it is possible to form an elemental composition map. When an electron from an outer atomic shell falls into an inner shell vacancy, the X-rays are emitted by the interaction between a charged beam and an electron in the shell. Thus, the X-ray energy is determined by the energy difference between these two shells, which is unique for each element. The energy of the X-rays emitted from a specimen can be measured by an energy-dispersive spectrometer. Fig 1.6 shows the working principal of the energy dispersive spectrometer. An EDX graph is normally represented as X-ray counts as a function of its energy in keV. Elements can be identified from the graph by their narrow peaks at the given energies.

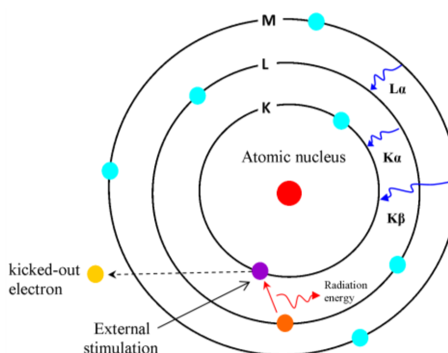

Figure 1.6: Principal of energy dispersive spectroscopy

1.5.3 Atomic Force Microscopy (AFM)

Atomic force microscopy (AFM) is a high-resolution microscopy technique which produces precise topographic images of a sample by scanning the surface with a nanometer-scale probe. A unique advantage of AFM is that it enables imaging with minimal sample preparation even in the air or liquid environment. However, it is advisable to use it under vacuum conditions to avoid the adsorption and desorption of atoms, which may lead to a change in the topography of the sample during the measurement. An AFM image is produced by exploring the interaction between the AFM tip and the scanned surface. Also, being capable to move in the three spatial dimensions, the AFM system can produce a three dimensional (3D) image with accuracy in the sub-nanometer range. Fig 1.7 shows the schematic diagram of the working principle of an AFM which is operated by measuring the force between a probe and the sample. Normally, the probe is a sharp tip, which is a 3-6 µm tall pyramid with 15-40 µm end radius. The AFM consists of three main parts: (1) a cantilever and a tip, the probe of the system (2) a piezoelectric transducer to control the cantilever movements in x, y and z direction; and (3) a laser and a detector to detect the cantilever deflection due to the interaction of the AFM tip with the scanned surface.

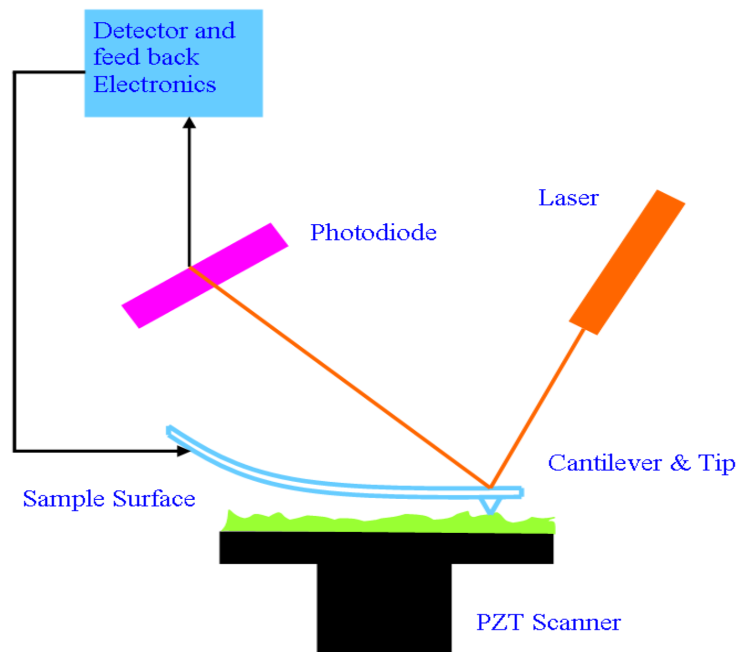

Figure 1.7: Schematic diagram on working principal of atomic force microscope

1.5.4 X-ray Diffraction (XRD) Analysis

The X-ray diffraction analysis is a tool used for identifying the atomic and molecular structures of a crystal, in which the crystalline atoms cause a beam of incident X-rays to diffract into many specific directions. The schematic of the working principal of X-ray diffraction analysis is shown in Fig 1.8. The main advantage of the X-ray diffraction analysis is that it discloses the presence of a compound as a whole in a sample but not in terms of its constituent chemical elements. The basic law that governs the diffraction method of structural analysis is the Bragg's law [Cullity (1967), Jenkins and Snyder (1996)].

According to this law, when a monochromatic X-ray impinges upon the atoms in a crystal lattice, each atom acts as a source of scattering. Thus, the crystal lattice acts as a series of parallel reflecting planes and the intensity of the reflected beam will be maximum at certain angles when the path difference between two reflected waves from two different planes is an integral multiple of the operating wavelength "λ". According to the Bragg's law, this condition is given by the relation [Cullity (1967)]

$$2d \sin\theta = n\lambda \tag{1.2}$$

where n is the order of diffraction, λ is the wavelength of the X-rays, d is the spacing between consecutive parallel planes and θ is the glancing angle.

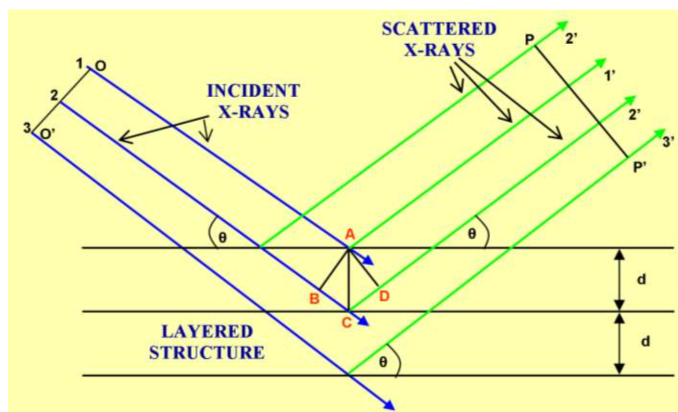

Figure 1.8: Schematic diagram for working principal of X-ray diffraction pattern

The X-ray diffraction studies give a whole range of information about the crystal structure, orientation, average crystalline size and stress in the films. The average grain size (D) of the sample can be calculated from the Debye Scherer's formula as [Cullity (1967)]

$$D = \frac{k\lambda}{\beta \cos\theta} \quad (1.3)$$

where k is a dimensionless shape factor with a value close to unity. The shape factor has a typical value of about 0.9, but varies with the actual shape of the crystallite and β is the full width at half maximum intensity in radians. The Scherrer equation is limited to nano-scale particles and it is not applicable to grains larger than about 0.1 to 0.2 μm.

1.5.5 Photoluminescence Spectrophotometer

Photoluminescence (PL) is a non-destructive technique widely used to detect and identify the near surface defects in the semiconductors. In the case of wide band gap semiconductor such as the ZnO, a UV laser is used to create the electron hole pairs within a depth of approximately 40 nm from the surface. The excess electron-hole pairs are then subsequently recombined through both the radiative and non-radiative transitions as shown in Fig.1.9. The radiative recombination results in a beam of emitted photons which are collected and analyzed by using a diffraction grating spectrometer and photomultiplier detector. The PL spectrum provides: (i) an indication of the relative optical activity of impurities and defects in the sample, and (ii) radiative transition energies which can be used to determine the electronic energy levels of the associated impurities and defects. The relative intensity of a peak in the PL spectrum is a function of the relative density of the associated impurity or defect and the radiative efficiency of the transition involved.

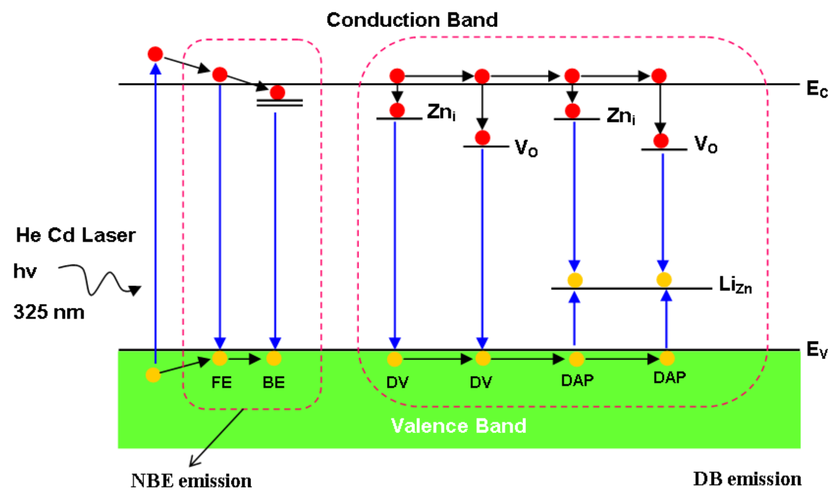

Figure 1.9: Different photoluminescence emission in the band gap of ZnO

1.6 Applications of ZnO Thin Film Based Electronic Devices

It is already mentioned earlier that ZnO thin film based devices can be used for many important electronic, optoelectronic and sensing applications. In this section, we will thus consider some important applications of the ZnO based nanoelectronic devices in the following:

Ultraviolet (UV) Photodetectors: The nanostructures of ZnO are expected to have good UV response due to their wide band gap energy and large surface area to volume ratio with the carrier and photon confinements in two dimensions. As a result, the devices based on ZnO nanostructures are expected to enhance the performance of UV photodetectors. The UV photoresponse of ZnO film was first observed by Mollow during 1950s [Mollow (1954)]. However, the research on ZnO based photodetectors flourished gradually since 1980s [Fabricius *et al*. (1986)]. Recently, many works have been reported on the photodetectors based on ZnO thin films [Liang *et al*. (2001), Basak *et al*. (2003), Zhu *et al*. (2008), Moon *et al*. (2005), Liu *et al*. (2010)]. However, only a limited amount of works on ZnO nanostructures based UV photodetectors are available in the literature [Lin *et al*. (2008), Zhai *et al*. (2009), Das *et al*. (2010b)].

Gas Sensors: ZnO nanostructures such as nanowires, nanorods, nanobelts and nanoparticles can be explored for gas sensing applications with better response than the bulk ZnO due to the improved granularity, porosity and ratio of the exposed surface area to the volume of the nanostructure ZnO materials [Huang and Choi (2007), Kyoung and Jang (2010)]. The variation of electrical properties of ZnO exposed to the reducing gases was first observed by Wagner [Wagner (1950)] in 1950. Since then, ZnO nanostructure based devices have been extensively studied for the detection of various gases including H_2, NO_2, and Hydrocarbons [Sadek *et al*. (2007)].

Thin Film Transistors: Recently, ZnO nanostructures are extensively used for the fabrication of transparent thin-film transistors (TFTs). Since ZnO is insensitive to visible light, ZnO based TFTs require no protective cover layer to prevent them from the visible light exposure. The transparent ZnO based TFTs were first demonstrated in 2003 by Nomura *et al.* [Nomura *et al*. (2003)]. Such invisible TFTs using ZnO as an active channel are observed to have much higher field effect mobilities (6-9 cm^2/Vs) than the mobility (0.5 cm^2/V-s) of the amorphous silicon transistors [Nomura *et al*. (2003)].

Piezoelectric Nanogenerators: The piezoelectric nanogenerator that converts mechanical energy into electricity was first demonstrated using ZnO nanowire arrays by Wang and Song [Wang and Song (2006)]. They [Wang and Song (2006)] demonstrated the conversion of nanoscale mechanical energy into electrical energy by means of ZnO NWs arrays by exploring the coupled piezoelectric and semiconducting dual properties of the ZnO material. Following this initial demonstration, ZnO nanogenerators have been developed for both the direct current and alternating current [Wang (2012)]. The output voltage of nanogenerators has been raised to 1.2V using an integration of millions of ZnO nanowires for driving a single nanowire-based UV/pH sensor [Wang (2012)].

Spintronics: ZnO is a very promising material for spintronics applications. The room-temperature ferromagnetism properties in the ZnO films doped with transition metals during growth by ion implantation have been reported [Pearton *et al*. (2006)]**.** Much of the research activity presently pursued in the area of spintronics is directed at demonstrating the device structures (e.g. spin-LED, spin-FET) that differentiate spin polarization distribution among the electron/hole population in the semiconductor [Ronning *et al.* (2004), Pearton *et al*. (2006)].

1.7 Metal-Semiconductor Electrical Contacts

Metal–semiconductor (M-S) contacts are important components in microelectronics. Depending on the work functions of the metal and semiconductors, the M-S junctions may exhibit either ohmic or rectifying type of electrical characteristics [Yu (1970), Rhoderick and Williams (1988), Tung (2001), Brillson and Lu (2011)]. In the ohmic M-S contacts, the junction behaves as a resistor in which current can flow in both directions through the junction depending on the polarity of the applied bias to the junction. On the hand, the rectifying M-S junctions can also be achieved in which the junction can behave similar to p^+-n or n^+-p diodes depending on whether the semiconductor is n-type or p-type. Thus, the current can flow only in one direction in the rectifying M-S junctions when the junction is forward biased (i.e. when higher potential is applied to the metal with respect to the semiconductor for the metal and n-type semiconductor junctions and the vice versa for the metal and p-type semiconductor junctions). The rectifying effect in the M-S contacts was first discovered by Braun [Braun (1874)] in 1874, who observed the one-way conduction in a galena (lead sulfide) crystal when contacted by a thin metal wire. Since then, an extensive

study has been carried out for formulating the electrical characteristics of the rectifying type M-S junctions in the literature [Cowley and Sze (1965), Rhoderick and Williams (1988), Sze (1981)]. The rectifying M-S contacts are also commonly known as Schottky junctions [Rhoderick and Williams (1988), Sze (1981)]. In order to use the metal-ZnO based systems in the thesis, some fundamental discussions on the ohmic and rectifying type of M-S junctions are presented in the following.

1.7.1 Metal-ZnO Ohmic Contacts

Ohmic contacts are required for all the ZnO based electronic and optoelectronic devices, thin film transistors (TFTs) [Nomura *et al*. (2003)], piezoelectric nanogenerators [Wang and Song (2006)], light emitting diodes (LEDs) [Choi *et al*. (2010)], solar cells [Xu *et al*. (2014)], and UV detectors [Liu *et al*. (2010)].

An ohmic contact is an M-S system with a zero or negative barrier height (defined as the difference between work function of the metal and the electron affinity of the semiconductor) [Sze (1981), Rhoderick and Williams (1988)] that should ideally have linear current-voltage relationship in both the forward and reverse bias regions. For obtaining an ohmic contact between a metal with work function $q\phi_m$ and semiconductor with work function $q\phi_s$, one is required to select the metal and semiconductor in such a way that the condition $q\phi_s > q\phi_m$ is satisfied when the semiconductor is *n*-type and $q\phi_s < q\phi_m$ when the semiconductor in the M-S system is *p*-type) [Sze (1981)]. Researchers have used several metals/combination of metals such as Al [Kim *et al.* (2004)], Ti/Al [Kim *et al*. (2002)], In [Akane *et al*. (2000)], Al/Au [Kim *et al*. (2009)], ITO [Tang *et al*. (2001)], Ti/Au [Lee *et al*.(2001)] and Zn/Au [Kim *et al*. (2005)] for forming ohmic contacts on n-ZnO nanostructures.

1.7.2 Metal-ZnO Schottky Contacts

The metal-ZnO based Schottky contacts have been the subject of interests for many ZnO based devices including thin film transistors (TFTs) [Nomura *et al*. (2003)], solar cells [Anta *et al*. (2012)], piezoelectric nanogenerator [Wang and Song (2006)], gas sensors [Huang and Choi (2007), Wang *et al.* (2009)] and ZnO based UV photodetectors [Lin *et al*. (2008), Zhai *et al*. (2009)]. However, the fundamental mechanisms governing the Schottky contact formation are still not fully clear and thus have remained the subject of current

research especially for ZnO thin film based Schottky devices [Allen (2008), Brillson and Lu (2011)]. This is largely due to the complex natures of nanostructured semiconductor surfaces with higher density of interface states as compared to their bulk ZnO counterpart.

The energy band diagram of a Schottky contact formed between a metal and a moderately doped n-type semiconductor (e.g. ZnO) is shown in Fig. 1.10, where ϕ_m (in eV) and ϕ_s (in eV) are the work functions of the metal and semiconductor respectively, and χ_s (in eV) is the electron affinity of the semiconductor. In general, in order to form a Schottky contact between a metal and a semiconductor, the condition $q\phi_m > q\phi_s$ is required to be satisfied when the semiconductor is *n*-type and the reverse condition (i.e. $q\phi_m < q\phi_s$) is to be satisfied is *p*-type semiconductor [Sze (1981)]. Since ZnO is inherently an n-type semiconductor, we are required to select a metal in such a way that $q\phi_m$ of the metal is greater than $q\phi_s$ of the ZnO for achieving the rectifying nature of metal-ZnO junction, as demonstrated in Fig 1.10 (a) before making the contact while the equilibrium energy band diagram of the Schottky M-S junction is shown in Fig. 1.10 (b). Such a M-S junction is termed as the **Schottky barrier** contact or simply the Schottky contact [Schottky (1938), Mead (1965), Sze (1981)] because the electrons in the metal side face a constant energy barrier $q\phi_B\,(=q(\phi_m-\chi_s))$, called the Schottky barrier height, while trying to flow from the metal to the semiconductor side. The quantity $qV_{bi}\,(=q(\phi_m-\phi_s))$ represents the energy barrier faced by the electrons in the n-type semiconductor while trying to flow from the semiconductor to the metal side under thermal equilibrium condition due to the band-bending or built-in voltage V_{bi} [Cowley *et al.* (1965), Neville and Mead (1970), Sze (1981)].

When a forward bias voltage V_F is applied to the Schottky M-S junction as shown in Fig. 1.11 (a), the potential barrier faced by the electron on the semiconductor side is reduced by qV_F thereby making the resultant energy barrier equal to $q\left(V_{bi}-V_F\right)$. The reduction in the energy barrier for electrons in the semiconductor side due to the applied bias causes more and more number of electrons to overcome the barrier easily and enter from the semiconductor to the metal side. On the other hand, when a reverse bias voltage $\left(V_R\right)$ is applied across the Schottky M-S junction, the flow of electrons from the semiconductor to the metal side is restricted by the increase in the energy barrier faced by

the electrons in the semiconductor from qV_{bi} at equilibrium condition to $q(V_{bi}+V_R)$under reverse bias operation [Sze (1981)] as shown in Fig.1.11 (b).

It may be mentioned that the Schottky barrier height $q\phi_B$ remains unchanged with the junction bias voltage and hence the number of electrons entering from the metal to semiconductor due thermionic emission remain same for all the bias conditions. Thus, the current in the metal-semiconductor Schottky contacts can be controlled by controlling the flow of the majority carriers (i.e. electrons) from the semiconductor to the metal side by changing the applied bias voltage. Since the flow of electrons from the semiconductor is negligible under reverse bias condition, the reverse bias current is mainly due to the flow of electrons from the metal to semiconductor side due to thermionic emission. Clearly, the reverse bias current can be reduced by increasing the Schottky barrier height $q\phi_B$ at the junction. In brief, the net current flow (i.e. opposite to the electron flow) occurs mainly in one direction (i.e. from metal to semiconductor) under forward biased condition and becomes negligibly small under reverse biased condition in the Schottky M-S junctions.

In general, ZnO thin film Schottky diodes are larger area contacts (with typical junction diameter of 10 μm-1mm diameter) which can be fabricated by using a variety of techniques, such as thermal evaporation, electron beam evaporation, sputtering, and pulse laser deposition. The deposition of metal is usually done in a high vacuum condition to avoid oxidation of the metal. A number of metals such as Pd (5.12), Pt (5.65), Au (5.10), Ag (4.26) [Wenckstern *et al.* (2006), Lajn *et al*. (2009), Mtangi *et al.* (2009), Brillson and Lu (2011)] etc. are reported in the literature for achieving good Schottky contact on ZnO films with the value of electron affinity varying between 3.7 eV [Majumdar and Banerji (2009)] and 4.35 eV [Brillson and Lu (2011].

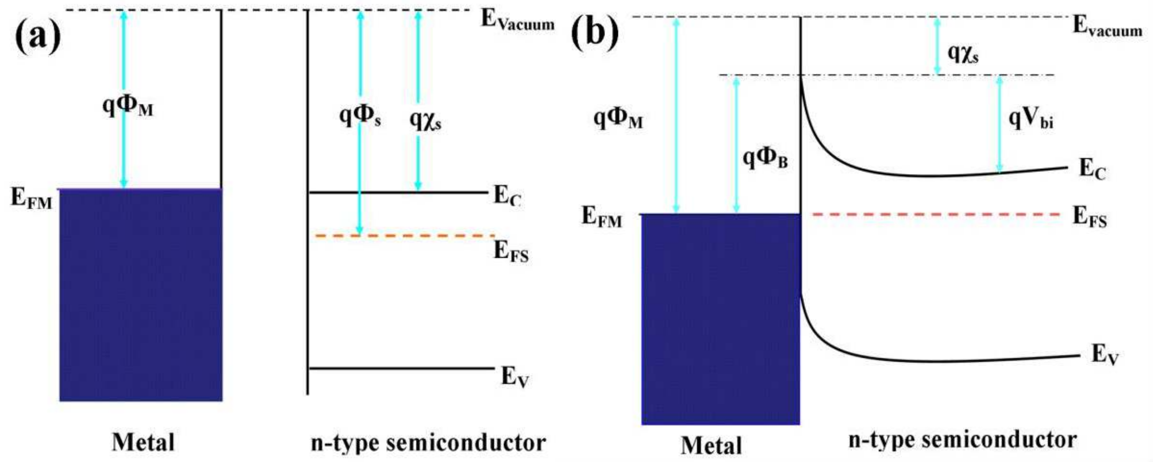

Figure 1.10: Energy band diagram of metal and n-type semiconductor **(a)** before contact **(b)** Schottky contact under thermal equilibrium

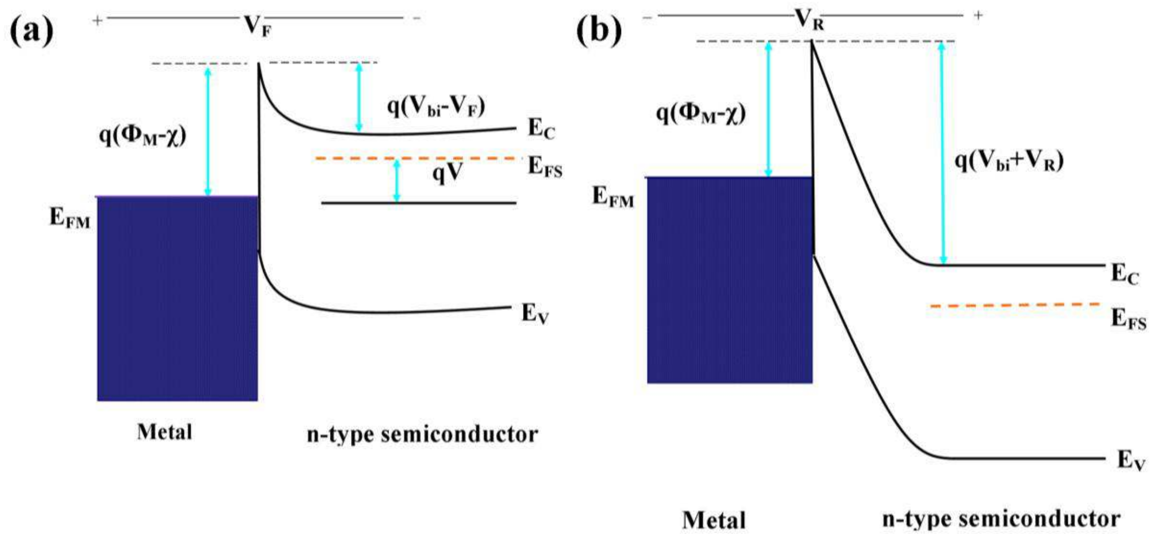

Figure 1.11: Energy band diagram of metal and n-type semiconductor **(a)** with applied forward bias **(b)** with applied reverse bias.

1.7.3 Heterojunctions

A “heterojunction” is a junction formed between two dissimilar semiconductors of different band gap energies [Anderson (1962), Sze (1981), Mönch (2001)]. The differences in the energy band gap and electron affinity between the two semiconductors result in the discontinuities or band offsets in the conduction and valence bands at the metallurgical junction that slow down the flow of carriers across the junction of the semiconductors involved in the heterojunctions [Anderson (1962), Perlmant and Feucht (1964), Sze (1981), Nixon and Davies (1990)]. The conduction and valence band offsets play a major role in the current transport properties of heterojunction diodes. Depending on the alignment of the energy bands of the semiconductors in the heterojunction diodes, they can be classified as (a) straddled or Type I alignment, (b) staggered or Type II alignment, and (c) broken gap alignment or Type III as shown in Fig.1.12.

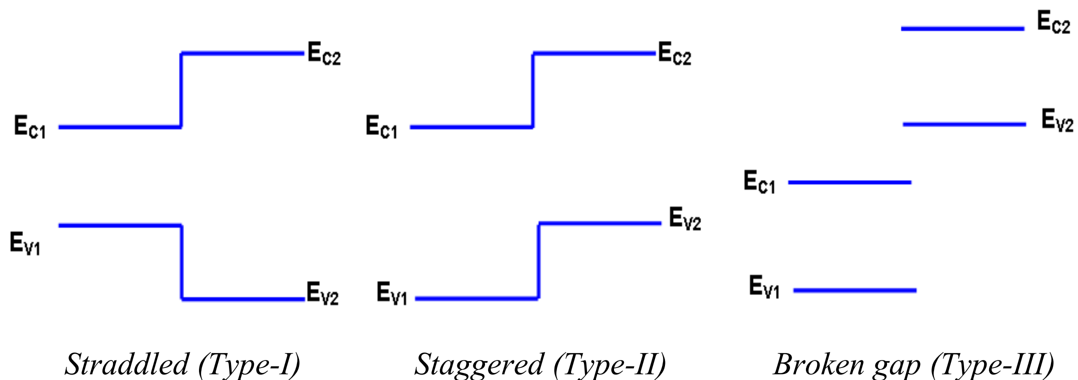

Figure 1.12: Different types of energy band alignments in heterojunction diodes

The first successful heterojunction structure of Ge/GaAs was developed by Anderson in 1960 [Anderson (1962), Sze (1981)]. He developed the electron affinity model, also known as the Anderson model [Anderson (1962), Sze (1981)], to determine the energy band diagram of heterojunctions at the interface to predict the current flow in heterojunction diodes. The model was based on the assumption of the ideal heterojunctions where the interface states are assumed to be zero at the heterojunction interface and current transport is assumed to be entirely by injection of carriers over the band offsets into the quasi-neutral region of the semiconductors. Although, this is rarely the case in the practical heterojunctions however, the Anderson model [Anderson (1962)] is generally used for

studying theoretical performance of the ideal heterojunctions. Among three configurations of the heterostructures mentioned earlier, the most commonly one is the type I heterojunction whose various parameters have been illustrated in terms of the Anderson's model in Fig 1.13.

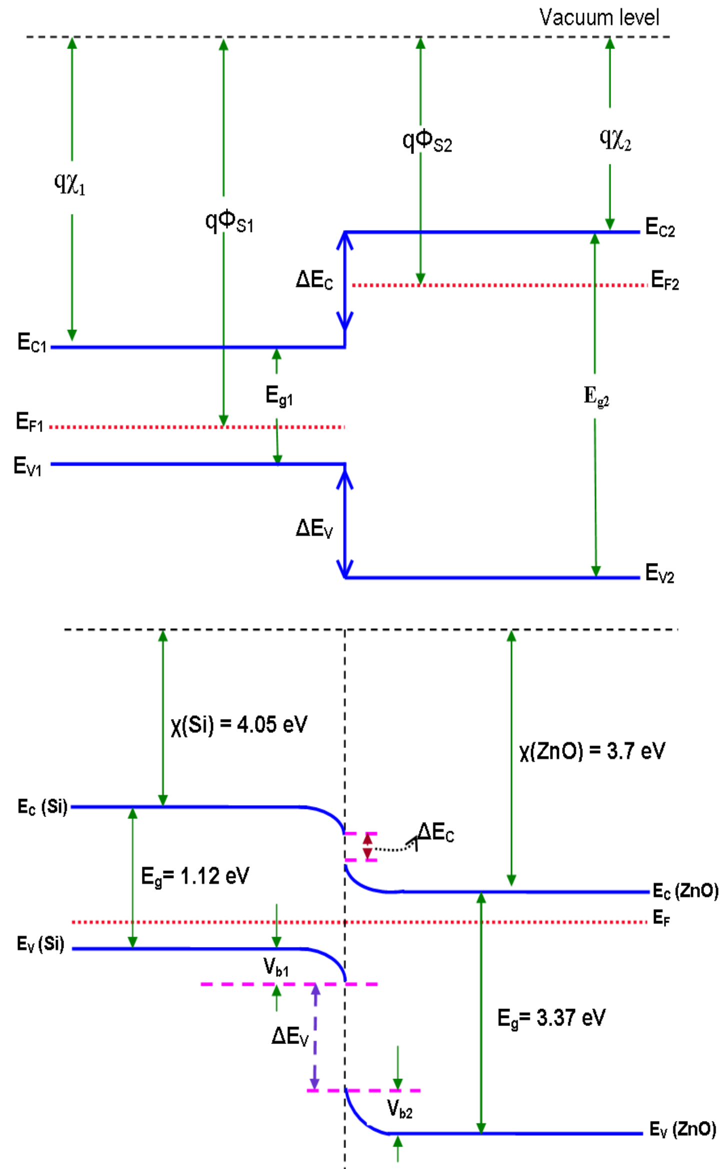

Figure 1.13: (a) Energy band diagram of two isolated semiconductors with different energy bandgap E_g, different work function $q\phi_s$ and different affinities $q\chi$ **(b)** The figure shows the equilibrium band of an ideal abrupt (n-ZnO/p-Si) heterojunction

Assuming that the two semiconductors 1 and 2 have the band gaps of E_{g1} and E_{g2} with $E_{g2} > E_{g1}$, electron affinities of χ_1 and χ_2, work functions of ϕ_1 and ϕ_2, doping

densities of N_1 and N_2, dielectric constants of ε_1 and ε_2 respectively, the various parameters of the Anderson model can be defined in the following [Sze (1981)].

$$\Delta E_C = \chi_1 - \chi_2 \tag{1.4}$$

$$\Delta E_V = (E_{g2} - E_{g1}) \pm \Delta E_C \tag{1.5}$$

$$V_{bi} = (\phi_1 - \phi_2) = (V_{b1} + V_{b2}) \tag{1.6}$$

$$\frac{V_{b1}}{V_{b2}} = \frac{N_2 \varepsilon_2}{N_1 \varepsilon_1} \tag{1.7}$$

In Eq.1.5, the negative sign for ΔE_C is used for type I and positive sign used for the type II alignment heterojunctions. According to the sign convention used for ΔE_V, positive value suggests that the energy of the valence band of semiconductor 1 is higher than that of semiconductor 2. The symbols V_{b1} and V_{b2} are used to denote the respective built-in voltage portions contributed by semiconductor 1 and 2 at thermal equilibrium to the total built-in (V_{bi}) voltage or the total band bending of the heterojunction. The ratio of band bending at each side of the semiconductor interface is given by Eq.1.7. Although, the Anderson's model can be used successfully for roughly predicting the band discontinuities of many heterojunctions, however, the I-V characteristics of the heterojunctions derived based on the this model usually do not agree with the experimental results [Sze (1981)]. This is due to the impractical assumptions of abrupt metallurgical junctions and the absence of any interface states in the Anderson's model. Further, in practical heterojunction diodes, current transport usually arises from a combination of carrier injection over the band offsets (through diffusion or thermionic emission), recombination of carriers in depletion region and tunneling of carriers into interface states [Sze (1981), Rhoderick and Williams (1988)] which are difficult to consider altogether in the theoretical modeling of the I-V characteristics of the Schottky diodes. Since the interface quality is strongly influenced by the choice of the metals, semiconductors and fabrication conditions of the heterojunctions, there is not even a single definite model for the I-V characteristics of heterojunctions which can take care of all the physical phenomena at the heterojunction interface.

1.8 Current Transport Mechanisms in the Metal/Semiconductor Systems

In this section, we will discuss different current transport mechanisms in the Schottky junctions formed between a metal and an n-type semiconductor as demonstrated in Fig. 1.14 where "V" is applied forward bias voltage and; E_V, E_C and E_F are the energies of the valence band, conduction band and Fermi level of the n-type semiconductor. Note that the Schottky barrier height $q\phi_B (=q(\phi_m - \chi_s))$ is ideally constant and independent of the biasing potential since both the ϕ_M and χ_s bias-independent parameters of the metal and semiconductor respectively. However, in reality, the practical barrier height differs from its ideal value of $q\phi_B$ due to the barrier inhomogeneity phenomenon [Werner and Güttler (1991)] discussed later in this chapter. That is why, the $q\phi_B$ has been replaced by $q\phi_{B,eff}$ in the Fig.1.14 just to signify that the measured barrier height is different from its ideal value in practical metal-semiconductor Schottky junctions. In any Schottky junction, the following four types of different carrier transport phenomena are responsible for the junction current [Schottky (1938), Mead (1965), Sze (1981), Brillson and Lu (2011)].

1) For a moderately doped semiconductor (e.g. Si with donor concentration $\leq 10^{17}$ cm^{-3}) where the barrier width is sufficiently large, the thermionic emission is the dominant transport mechanism for electron transport over the barrier. In this process, electrons with kinetic energy more than the potential barrier of the respected side of the junction may enter from one side to the other side and contribute to the total current flowing through the junction [Sze (1981)].

2) When the barrier width is much smaller due to larger doping in the semiconductor, current in the devices may occur by the quantum mechanical tunneling of the electrons through the barrier. In this case some electrons with energy in the vicinity of the Fermi energy level may be excited to higher energy level by emission and then finally tunneled through the barrier easily due to smaller barrier thickness at higher energy level. This is commonly known as Thermionic Field Emission (TFE) phenomenon. Both the field emission (FE) and TFE carrier transport processes are responsible for contributing current to an ohmic M-S junction [Sze (1981)].

3) Current in an M-S system may also be contributed by the recombination of the carriers in depletion region similarly as that in a p-n junction [Sze (1981)].

4) Current in the M-S system may also be resulted from the injection of the holes from the metal into the semiconductor which is equivalent to the recombination of electrons and holes in the neutral regions of a p-n junction [Sze (1981)].

In addition to the above mechanisms, there may be an edge leakage current due to the high electric field near the junction or interface current due to interface traps at the metal-semiconductor interface [Sze (1981), Barret and Muret (1983)]

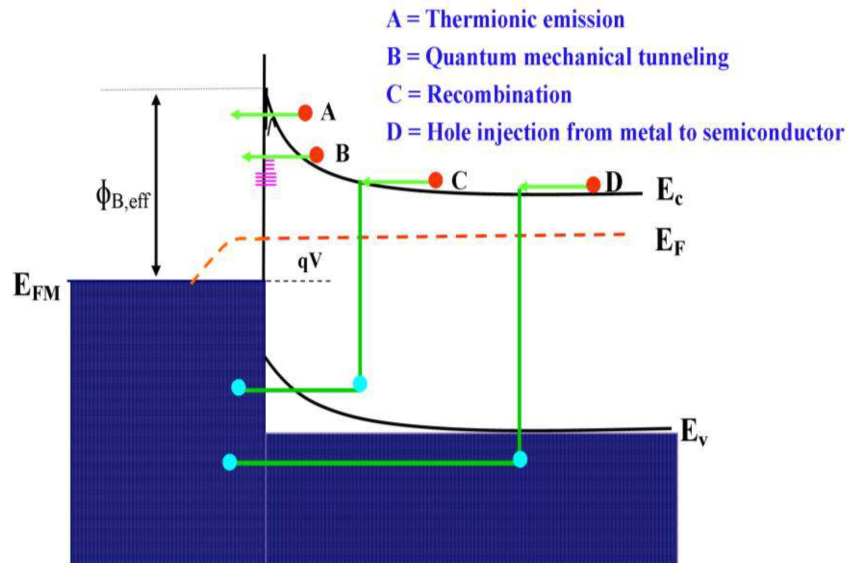

Figure 1.14: Different current transport mechanism across M-S junction

1.9 Electrical Characteristics of Metal-Semiconductor Junctions

In this section, we will briefly introduce the determination of various electrical parameters of the M-S Schottky junctions from its current (I)-voltage (V) characteristics as discussed below.

1.9.1 Current-Voltage (I-V) Characteristics

In 1942, Hans Bethe [Bethe (1942)] first derived the I-V characteristics of the Schottky junction diodes by using the thermionic emission theory. Bethe's thermionic theory is

based on the following assumptions [Sze (1981)]: **(i)** the barrier height $q\phi_B (= q(\phi_m - \chi_s)) >> kT$; **(ii)** the plane which determines the thermionic emission of electrons from the n-type semiconductor (for a metal and n-type semiconductor Schottky junction) to the metal over the potential barrier and the electrons from metal to semiconductor over the Schottky barrier is always under thermal equilibrium condition; and **(iii)** the emission probability is too low to disturb the thermal equilibrium [Schottky (1938), Mead (1965), Sze (1981)] under all biasing conditions of the junction.

Based on the thermionic theory of Bethe [Bethe (1942)], the expression for the current density at the metal-semiconductor junction of the Schottky diodes can be given by [Bethe (1942), Sze (1981)]

$$J = \left[A^* T^2 \exp\left(-\frac{q\phi_{B,eff}}{kT} \right) \right] \left[\exp\left(\frac{qV}{\eta kT} \right) - 1 \right] \tag{1.8}$$

or

$$J = J_S \left[\exp\left(\frac{qV}{\eta kT} \right) - 1 \right] \tag{1.9}$$

where

$$J_S = A^* T^2 \exp\left(-\frac{q\phi_{B,eff}}{kT} \right) \tag{1.10}$$

is the reverse saturation current density, $\phi_{B,eff} = V_n + V_{bi}$ is the barrier height, $V_n = E_C - E_F$ in the neutral region of the semiconductor, V_{bi} is the built-in potential, η is the ideality factor of the Schottky junction, and

$$A^* = \frac{4\pi q m_e^* k^2}{h^3} \tag{1.11}$$

is the effective ***Richardson constant*** for thermionic emission of electron over the Schottky barrier where m_e^* is the effective density of mass of electrons in the semiconductor, k is the Boltzmann constant and h is the Plank's constant. The value of the Richardson constant for ZnO is $\sim 32 Acm^{-2}K^{-2}$ (for $m_e^* = 0.27 m_0$) [Mtangi *et al*. (2009), Sarpatwari *et*

al. (2009), Lajn *et al*. (2009)]. If the Schottky contact area is "A", then the total current I of the device can be given by

$$I = JA = AJ_S\left[\exp\left(\frac{qV}{\eta kT}\right)-1\right] = I_S\left[\exp\left(\frac{qV}{\eta kT}\right)-1\right] \tag{1.12}$$

where

$$I_S = AJ_S = AA^*T^2\,exp\left(-\frac{q\phi_{B,eff}}{kT}\right) \tag{1.13}$$

where I_S is the reverse saturation current.

(a) Determination of reverse saturation current, barrier height and ideality factors:

For moderately doped semiconductors, the forward biased I-V characteristics can be approximately obtained from Eq. (1.9) for $V > \frac{3kT}{q}$ as

$$I = I_S\left[exp\left(\frac{qV}{\eta kT}\right)-1\right] \approx I_S\,exp\left(\frac{qV}{\eta kT}\right) \tag{1.14}$$

Taking natural logarithm in both sides of Eq. (1.14), we can write

$$ln(I) = ln(I_S) + \frac{qV}{\eta kT} \tag{1.15}$$

It is observed from Eq. (1.15) that the saturation current I_S can be determined by extrapolating the current from the log-linear region to $V = 0$. Since I_S is constant for a particular device, the ideality factor can be obtained by differentiating Eq. (1.15) with respect to V as

$$\eta = \frac{q}{kT}\frac{\partial V}{\partial \ln(I)} \tag{1.16}$$

Eq. (1.16) clearly shows that the ideality factor can be determined from the slope of the ln (I) versus V plot.

Once the reverse saturation current density is known, the effective barrier height can be written as

$$\phi_{B,eff} = \frac{kT}{q} ln\left(\frac{AA^* T^2}{I_s}\right) \tag{1.17}$$

(b) Determination of Richardson constant

The Richardson constant (A^*) is a fundamental parameter that characterizes the thermionic emission process in Schottky contacts [Crowell (1965), Sze (1981), Bhuiyan (1988)]. It is observed from Eq. (1.11) that the Richardson constant depends upon the electron effective mass which is a function of temperature [Crowell (1965), Allen (2008), Sarpatwari (2009)]. Thus, it is important to determine the actual value of the Richardson constant in a range of temperatures in which barrier height is evaluated. Generally, Schottky contacts are often far from ideal and the reported Richardson constant values are significantly lower than the theoretical value [Mtangi *et al*. (2009), Allen *et al*. (2009), Sarpatwari *et al*. (2009)].

After re-arranging the terms in Eq. (1.13) and taking natural logarithm we can obtain

$$ln\left(\frac{I_S}{T^2}\right) = ln\ AA^* - \frac{q\phi_{B,eff}}{kT} \tag{1.18}$$

The Richardson constant (A^*) is extracted from the so-called Richardson plot defined as a plot of $ln\left(\frac{I_S}{T^2}\right)$ vs. $\frac{q}{kT}$. The A^* is determined for a practical Schottky diode by using the Richardson plot by using the measured current-voltage characteristics at different operating temperatures [Sze (1981), Werner and Güttler (1991)].

From the measured temperature-dependent current-voltage (I-V-T) characteristics, the saturation current and barrier height are estimated first at different temperatures by following the methodology discussed above. Then the Richardson plot is drawn as per Eq. (1.18). Extrapolating the plot to the y-axis, we may determine the intercept which can be used to determine the Richardson constant as

$$A^* = \frac{exp\ (Intercept)}{A} \tag{1.19}$$

1.9.2 Effect of Barrier Inhomogenity at the Metal-Semiconductor Interface on the Electrical Characteristics of Schottky Junction:

As discussed earlier, the Schottky barrier $q\phi_B (= q(\phi_m - \chi_s))$ should be constant throughout the Schottky junction interface. However, in practice barrier height is a strong function of operating temperature and bias voltage of the device due to a phenomenon known as barrier inhomogeneity at any heterojunction interface in general, and at MS Schottky junction interface in particular. The barrier inhomogeneity phenomenon, in general, refers to the non-uniform random distribution of the spatial barrier height across the metal-semiconductor interface of a Schottky junction due to surface roughness, structural defects, surface contamination, or intrinsic point defects in the semiconductor [Werner and Güttler (1991), Tung (1992), Schmitsdorf *et al*. (1997), Mönch (1999)]. The assumption of a constant barrier height is applicable for an ideal metal-semiconductor Schottky junction where the interface is assumed to be an atomically flat surface. On the other hand, in any practical (non-ideal) metal-semiconductor junction, the interface between the metal and semiconductor is not atomically flat, but rough with spatial fluctuations of the built-in voltage, and the Schottky barrier height [Werner and Güttler (1991)] due to the thickness modulations of the metal as well as atomic steps, dislocations, and grain boundaries in the metal. Further, the thermionic field emission at metallic diffusion spikes with narrow radii of curvature may also result in a local barrier lowering thereby causing fluctuations in the built-in voltage and the Schottky barrier height in the practical Schottky devices. In brief, instead of a constant value of the barrier height at every point of the metal-semiconductor interface as per the Schottky-Mott theory [Sze (1981)], the barrier height takes on different values at different points of the junction interface in a random manner due to this barrier inhomogeneity phenomenon [Werner and Güttler (1991), Allen (2008), Sarpatwari (2009)] as demonstrated in Fig.1.15. Since metal-semiconductor junction is also a heterojunction, the concept of barrier height inhomogeneity is also applicable for the heterojunction devices.

Werner and Güttler [Werner and Güttler (1991)] developed a model for determining the Schottky barrier fluctuations caused by spatial barrier inhomogeneities in a length scale less than the depletion width W_d. The shape and position of the crests in the potential "mountains" shown in Fig.1.15 depend on bias voltage and therefore cause non-idealities in I-V characteristics. To include the randomness in the spatial barrier height across the

Schottky junction interface, they [Werner and Güttler (1991)] assumed the following Gaussian distribution $P(\phi_{B,eff})$ function for the barrier heights with a mean value $\phi_{B0,m}$ and a standard deviation σ_0 at zero bias condition:

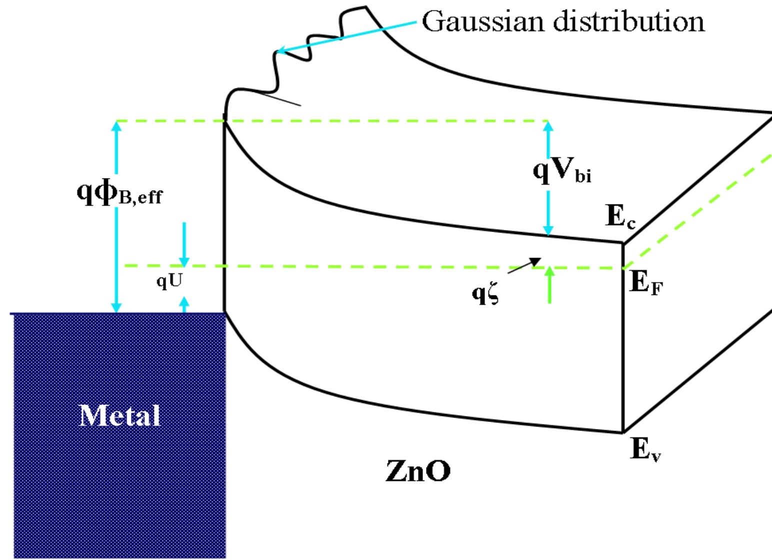

Figure 1.15: The Gaussian distribution of barrier heights across MS interface reproduced from the literature [Werner and Güttler (1991)].

$$P(\phi_{B,eff}) = \frac{1}{\sigma_0\sqrt{2\pi}} \exp\left[-\frac{(\phi_{B,eff} - \phi_{B0,m})^2}{2\sigma_0^2}\right] \tag{1.20}$$

where $1/\sigma_0\sqrt{2\pi}$ is the normalization constant for the Gaussian barrier height distribution. Now, the total current at the M-S interface is given by following relation:

$$I(V) = \int_{-\infty}^{+\infty} I(\phi_{B,eff}, V) P(\phi_{B,eff}) d\phi_{B,eff} \tag{1.21}$$

where $I(\phi_{B,eff}, V)$ is the current at bias V for the Schottky barrier height $\phi_{B,eff}$ based on thermionic emission model and $P(\phi_{B,eff})$ is the associated probability distribution function described by Eq. (1.20) for barrier height. Putting the value of $I(\phi_{B,eff}, V)$ from Eq. (1.12) and $P(\phi_{B,eff})$ from (1.20) in Eq. (1.21) and performing integration, Werner and Güttler

[Werner and Güttler (1991)] expressed the current $I(V)$ through the Schottky barrier at a forward bias V similar to Eq. (1.12) but with the modified barrier height and ideality factor as

$$I(V) = I_0 \exp\left(\frac{qV}{kT\eta(T)}\right)\left[1 - \exp\left(\frac{-qV}{kT}\right)\right] \tag{1.22}$$

where

$$I_0 = AA^* T^2 \, exp\left(\frac{-q\phi_{B.eff}(T)}{kT}\right) \tag{1.23}$$

where $\phi_{B,eff}(T)$ and $\eta(T)$ are the apparent barrier height and apparent ideality factor respectively which are defined as [Werner and Güttler (1991)]

$$\phi_{B,eff}(T) = \phi_{B0,m}(T=0) - \frac{q\sigma_0^2}{2kT} \tag{1.24}$$

$$\left(\frac{1}{\eta(T)} - 1\right) = \rho_1 - \frac{q\rho_2}{2kT} \tag{1.25}$$

$$\phi_{B,m}(V) = \phi_{B0,m} + \rho_1 V \tag{1.26}$$

$$\sigma^2(V) = \sigma_0^2 + \rho_2 V \tag{1.27}$$

where $\phi_{B0,m}$ is the mean barrier height and σ_0 is the linearly bias dependent on Gaussian parameters, ρ_1 and ρ_2 are voltage coefficient which may be dependent on temperature T and they quantify the voltage deformation of barrier height distribution.

The modified Richardson constant:

After performing barrier inhomogeneity corrections on I-V-T relation, the Richardson constant will get modified and calculated by using modified equation as given below [Mtangi *et al*. (2009), Allen *et al*. (2009)]:

$$\ln\left(\frac{I_0}{T^2}\right) - \left(\frac{q^2\sigma_0{}^2}{2(kT)^2}\right) = \ln\left(AA^*\right) - \frac{q\phi_{B0,m}(T=0)}{kT} \tag{1.28}$$

A plot between $\ln\left(I_0/T^2\right)-q^2\sigma_0{}^2/2(kT)^2$ versus q/kT gives a straight line with the slope giving the mean barrier height and intercept giving the modified Richardson constant.

1.9.3 Capacitance-Voltage (C-V) Characteristics

Capacitance vs. voltage (C-V) measurements is commonly used for electrical characterization of Schottky diodes as well as of the semiconductor material itself [Chang and Sze (1970), Sze (1981), Werner *et al*. (1988), Chattopadhyay and Haldar (2001)]. As we know that the depletion region of the Schottky contact entirely lies within the semiconductor and consists of space charge region with ionized donors which are largely unscreened by mobile carriers. The depletion region thus forms a "parallel plate like" capacitor with the metal and the undepleted bulk of the semiconductor as the two plates and the depletion width as the distance between the two plates [Allen (2008)]. Since, the width of the depletion region (W_d) is changed with an applied external bias voltage (V) to the Schottky junction, the capacitor is also expected to change with the bias voltage. The expression for the bias voltage dependent depletion region of the metal and n-type semiconductor based Schottky junction device can be given by [Sze (1981), Rhoderick and Williams (1988)]

$$W_d=\sqrt{\frac{2\varepsilon_s\varepsilon_0}{qN_D}\left(V_{bi}-\frac{kT}{q}-V\right)} \tag{1.29}$$

where N_D and ε_s are the donor concentration and the relative dielectric constant of the semiconductor respectively and ε_0 is the permittivity of the free space. The total space charge Q_{sc} in the depletion region is given by

$$Q_{sc}=qN_DW_dA \tag{1.30}$$

where A is the area of the contact. The small-signal capacitance of the Schottky junction is then given by [Allen (2008)].

$$C=\frac{dQ_{sc}}{dV}=A\sqrt{\frac{q\varepsilon_s\varepsilon_0N_D}{2\left(V_{bi}-\frac{kT}{q}-V\right)}} \tag{1.31}$$

This can also be written as:

$$\frac{A^2}{C^2} = \left(\frac{2}{q\varepsilon_s \varepsilon_0 N_D} \right) \left(V_{bi} - \frac{kT}{q} - V \right) \qquad (1.32)$$

Clearly, if the measured values of A^2/C^2 is plotted as a function of the applied bias voltage "V" by applying a small a. c signal, we will get a straight line whose slope can give the effective donor concentration of the semiconductor described by [Allen (2008)].

$$N_D = -\frac{2}{q\varepsilon_s \varepsilon_0 A^2} \left[\frac{d}{dV} \left(1/C^2 \right) \right]^{-1} \qquad (1.33)$$

Further, the built-in voltage V_{bi} can be obtained from the intercept of the slope with the A^2/C^2 axis. Once the V_{bi} is determined, the barrier height can also be estimated as $\phi_{B,eff} = V_n + V_{bi}$. In the presence of the barrier inhomogeneity, the estimated built-in potential of the Schottky contacts from the C-V characteristics may give the average value of V_{bi}. Some authors [Wenckstern *et al*. (2006)] have argued that the capacitance measurements are insensitive to potential fluctuations of a length scale less than W_d and therefore the barrier height determined by the C-V technique represents the mean value of barrier height i.e. $\phi_{B0,m}$.

1.10 Metal-Semiconductor Contact Based Photodetectors

In recent years, ZnO thin films based ultraviolet (UV) photodetectors have drawn considerable attention of the researchers because of the low material cost, easy availability, environment-friendly nature and bio-compatible characteristics of ZnO as discussed earlier [Zhai *et al*. (2009), Liu *et al*. (2010), Ali and Chakrabarti (2010)]. A number of ZnO-based UV detector structure including p-n junction photodiodes both in the homojunction and heterojunction forms [Kim *et al*. (2001), Alivov *et al*. (2005), Lopatiuk *et al*. (2006), Wang *et al.* (2007), Liu *et al*. (2010), Bacaksiz *et al*. (2010)], photoconductors [Basak *et al*. (2003), Liu *et al*. (2007)], Metal-insulator-semiconductor (MIS) photodetectors [Young *et al.* (2007)], metal-semiconductor-metal (MSM) photodiodes [Lin *et al*. (2005), Young *et al*. (2006), Li *et al*. (2006), Ali and Chakrabarti (2010)] and Schottky photodiodes [Liang *et al*. (2001), Oh *et al*. (2006), Endo *et al*. (2007), Nakano *et al*. (2008), Kim *et al.* (2010),

Das *et al*. (2010b)] have been reported in the literature. Among them, the ZnO MSM structure based UV detectors have drawn considerable attention in recent times because of its simple structure, ease of fabrication and integration techniques, and low capacitance per unit area [Lin *et al*. (2005), Ali and Chakrabarti (2010)]. Despite the inherently fast nature due to the low capacitance per unit area, the poor responsivity of the MSM photodiodes due to the small active light collecting region (caused by the shadowing of electrode metallization) is the major drawback of these devices [Liu *et al*. (2010)]. In comparison with the photoconductor and MSM structures, the Schottky photodiodes, in general, have higher quantum efficiency, lower dark current and higher UV/visible contrast [Liu *et al*. (2010)]. While ZnO based Schottky photodiodes consist of a simple Schottky metal contact on the ZnO film, the MSM structures can be viewed as two Schottky photodiodes structures connected back-to-back [Liu *et al*. (2010), Ali and Chakrabarti (2010)]. Thus, the ZnO Schottky photodiodes is simpler in structure with higher expected photo response than the MSM. Fig 1.16 shows different schematic structures of photoconductors, Schottky photodiodes, MSM photodetector and Metal-Insulator-Semiconductor (MIS) photodetectors.

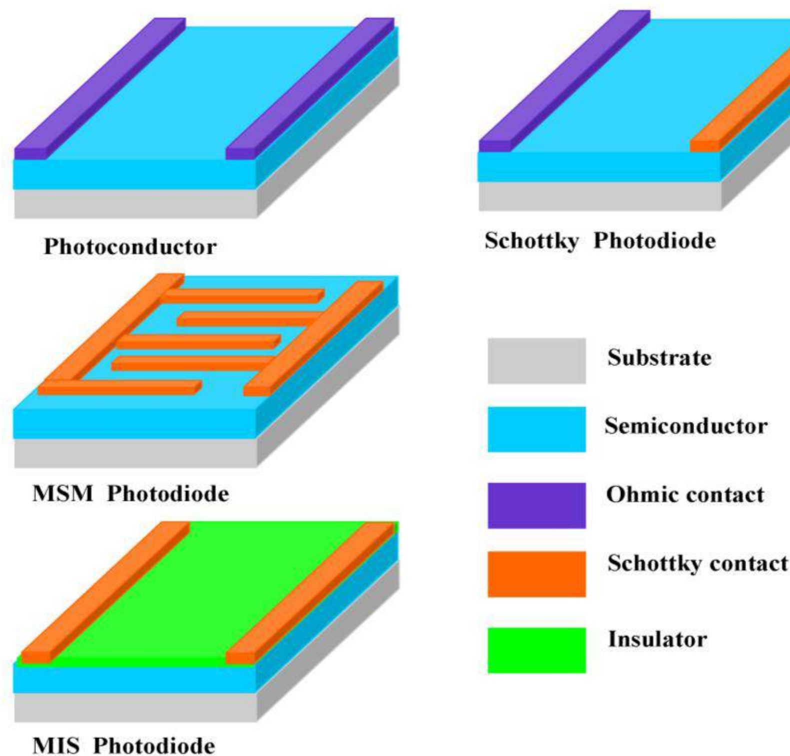

Figure 1.16: Schematic diagram of different photodetectors structure

Nowadays, Schottky photodiodes based on ZnO nanostructures are of great interests for the UV detection applications due to their high speed and low noise performance, in addition to their large surface-to-volume ratio with the carrier and photon confinements in two dimensions, superior stability owing to high crystallinity and possible surface functionalization with target-specific receptor species [Liu *et al*. (2010)]. Further, Schottky contacts with a large barrier height is generally preferred in photodetection operation since it leads to small leakage current and high breakdown voltage thereby improving the responsivity and contrast ratio of Schottky photodiodes.

The general principle of operation of metal-semiconductor Schottky contact based photodetectors involves two basic steps:

- The light signal (to be detected) consisting of photons with energy greater than the bandgap energy $(h\nu >> E_g)$ of the semiconductor is allowed to be absorbed in a selected region, called the active region of the photodetector.
- The absorbed photons create excess electron-hole pairs $(h\nu \rightarrow h^+ + e^-)$ in the active region. A suitable electric field is then applied across the device to collect the photo-generated electrons and holes in the active region so that a resultant current proportional to the incident optical power is available in the external circuit.
- The bandgap energy E_g of the semiconductor of the active region determines the wavelength (i.e. visible or ultraviolet) of operation of the detector by the following relation: $\lambda(\mu m) = \frac{1.24}{E_g(eV)}$

1.11 Scope of the Thesis

The basic objective of present thesis is to investigate the electrical characteristics of some ZnO nanostructures based devices grown on Si substrates (for their compatibility with CMOS technology) for electronic and optoelectronics applications. The scope of the work has also been extended to explore the UV detection characteristics of ZnO nanostructures based Schottky diodes grown on n-Si substrates by low-cost self assembly methods. The present dissertation consists of seven chapters including the present one entitled as "Introduction". The contents of remaining chapters are as follows:

Chapter 2 includes the review of some of the major state-of-the-art-research works in the related area of ZnO thin film based devices reported in the literature. The latest trends in the development of various ZnO based metal-semiconductor contacts, heterojunction diodes and their applications for UV photodetectors are reviewed in details. Based on the literature survey and keeping in the view of various lacunas, the motivation behind the present study is outlines at the end of this chapter.

Chapter 3 reports fabrication and characterization of Pd/ZnO thin film Schottky diodes grown on n-Si substrates by thermal evaporation method. The surface morphology, crystalline structure and optical properties of ZnO thin film have been determined by FESEM image, XRD pattern and PL spectrum respectively. The donor concentration of ZnO thin film has been calculated by room temperature C-V characteristics. The values of electrical parameters such as barrier height, and ideality factor have been determined from the measured room temperature I-V characteristics. The series resistance of the Schottky diodes has been estimated and compared by using the Cheung-Cheung method and Norde's method. Further, the temperature-dependent I-V characteristics of Pd Schottky contacts grown on ZnO thin film have been analyzed in the temperature range from 300 to 423K. Finally, the value of Richardson constant and mean barrier height are calculated by taking phenomenon of Gaussian distribution of barrier heights as proposed by Werner and Güttler [Werner and Güttler (1991)] into consideration.

Chapter 4 is devoted to investigate the effects of the ZnO, Sn and Zn seed (or buffer) layers on the electrical characteristics of Pd/ZnO thin film Schottky contacts grown on n-Si substrates by thermal evaporation method. Seed layers of ZnO, Sn and Zn are deposited on n-Si substrates before the deposition of ZnO thin films by thermal evaporation method. We have divided this chapter into two parts. In the first part, the effects of the ZnO seed layer on the electrical characteristics of Pd/ZnO thin film Schottky contacts grown on n-Si substrates by thermal evaporation method have been discussed. The second part contains the effects of Sn and Zn metal seed layers on electrical parameter such as rectification ratio, barrier height and ideality factor of Pd/ZnO thin film Schottky contacts grown on n-Si substrates. The electrical characteristics of all three Pd/ZnO Schottky diodes with Sn, Zn and ZnO seed layer are compared with Pd/ZnO thin film Schottky diodes grown on bare n-Si substrates already discussed in Chapter 3. The change in surface morphology, chemical composition and crystalline structure of ZnO thin films grown on

the ZnO, Sn and Zn seed layers have also been studied by FESEM images, EDS spectrum and XRD pattern respectively.

Chapter 5 presents the ultraviolet detection characteristics of Pd Schottky diodes grown on ZnO nanoparticles (NPs) by thermal evaporation method. The ZnO nanoparticles have been synthesized on Sn coated n-Si substrates by thermal evaporation method as described earlier in Chapter-4. The optical characteristics of ZnO nanoparticles have been determined by PL spectroscopy. The I-V characteristics of the Schottky diodes have been studied and analyzed under both the dark and UV illuminated conditions. The responsivity, contrast ratio, detectivity and quantum efficiency of the Pd/ZnO NPs based Schottky photodiodes have determined and compared with other reported results. The UV detection mechanism on the surface of ZnO nanoparticles has been discussed in details.

Chapter 6 reports the fabrication and characterization of n-ZnO nanowires (NWs) /p-Si based heterojunction diodes by thermal evaporation method. The n-ZnO nanowires are synthesized on 1% Al doped ZnO (AZO) coated p-Si substrates by thermal oxidation of vacuum deposited Zn at 600 ºC for the duration of 60 minutes. The surface morphology and crystalline structure of ZnO nanowires have been studied by analyzing the FESEM images and XRD pattern respectively. The optical properties of ZnO nanowires have been examined by PL spectroscopy at room temperature. The current-transport mechanism at the n-ZnO/p-Si heterojunction interface has been investigated by Anderson model. The measured temperature-dependent I-V and room temperature C-V characteristics have been analyzed for estimating various parameters of the n-ZnO NWs/p-Si heterojunction diodes under consideration. Finally, the value of Richardson constant is calculated by including the effects of barrier height inhomogenity at the n-ZnO/p-Si interface. The distribution of density of interface states in the band gap of ZnO has also been discussed.

Chapter 7 summarizes some major outcomes and finding of the thesis. This chapter has been devoted to conclude the major findings from the discussions of the previous chapters of the present thesis. Finally, based on the constraints and limitations of the present study, an outline for the further scope of the work in the related area has been presented at the end of this chapter.